CMS Physics Analysis Summary

Contact: cms-pag-conveners-higgs@cern.ch 2015/01/27

Search for new physics in final states with low transverse energy photon and missing transverse energy in proton-proton collisions at $\sqrt{s} = 8$ TeV

The CMS Collaboration

Abstract

We present a search for new physics in the final state of a low transverse energy photon and missing transverse energy using 7.3 fb^{-1} of $\sqrt{s} = 8$ TeV LHC proton-proton collisions collected with the Compact Muon Solenoid (CMS) detector. This analysis extends the high-energy single-photon searches to a lower-energy regime. In the absence of deviations from the standard model predictions, limits are set on the production cross section of exotic decays of the Higgs boson. We have also analyzed the phase space consisting of a photon with a transverse energy of at least 45 GeV and missing transverse energy in a model independent way by varying the selection requirements on the missing transverse energy and transverse mass. We set upper limits at the 95% confidence level on the production cross section of possible processes appearing in this final state.

1 Introduction

The final state consisting of a low transverse energy photon and low missing transverse energy ($\not\!\!E_T$) (also called the "monophoton" final state) can be used to constrain a variety of extensions of the standard model (SM). One such promising extension is supersymmetry (SUSY) [1–7], which has the attractive feature of stabilizing the radiative corrections to the Higgs boson mass (m_h), while also providing a natural dark matter (DM) particle candidate (χ) in the form of the lightest supersymmetric particle (LSP).

In SUSY scenarios where the SUSY breaking scale is low ($\sqrt{f} \sim$ TeV) the newly discovered Higgs boson ($m_h = 125\,\text{GeV}$) [8, 9] may decay into a gravitino ($\widetilde{\text{G}}$) and neutralino ($\widetilde{\chi}_1^0$), with the neutralino subsequently decaying into a gravitino and a photon [10]. In this model, the gravitino is the LSP and the neutralino is the next to lightest supersymmetric particle (NLSP). Figure 1 shows the Feynman diagram for this process.

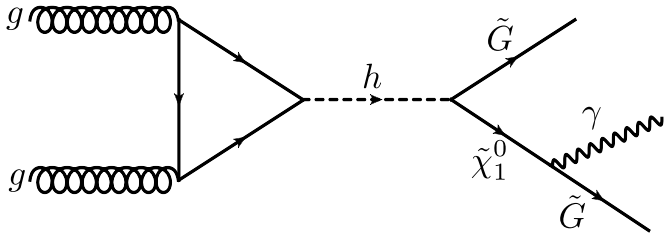

Figure 1: Feynman diagrams of a Higgs boson decay to gravitino LSP and a neutralino NLSP, which subsequently decays to a gravitino and photon.

This decay mode produces a single isolated photon and $\not\!\!E_T$ from the undetected gravitinos. If $m_{\widetilde{\chi}_1^0} < m_h/2$, the decay process $h \to \widetilde{\chi}_1^0\widetilde{\chi}_1^0 \to \gamma\gamma + \not\!\!E_T$ would dominate. Therefore the kinematic region of interest for this search is $m_h/2 < m_{\widetilde{\chi}_1^0} < m_h$. Furthermore, since $m_h = 125\,\text{GeV}$, the photon transverse energy (E_T^γ) and $\not\!\!E_T$ will be relatively low.

In this document, we present a search for new physics in the low-E_T photon+$\not\!\!E_T$ final state, using an integrated luminosity at $7.3\,\text{fb}^{-1}$ of $\sqrt{s} = 8\,\text{TeV}$ LHC pp collision data collected with the CMS detector. This study is the first CMS search conducted in this low energy regime and it complements and expands upon previous high-energy monophoton searches for new physics conducted at the LHC [11, 12]. The results are interpreted in terms of the low-scale SUSY breaking model, as well as in a model independent manner.

2 CMS Detector and Reconstruction

The central feature of the CMS apparatus is a superconducting solenoid of 6 m internal diameter, providing a magnetic field of 3.8 T. Within the superconducting solenoid volume are a silicon pixel and strip tracker, a lead tungstate crystal electromagnetic calorimeter (ECAL), and a brass/scintillator hadron calorimeter (HCAL), each composed of a barrel and two endcap sections. The ECAL is made up of nearly 76,000 crystals and provides a pseudorapidity coverage up to $|\eta| < 1.48$ in the barrel region while $1.48 < |\eta| < 3.0$ is the endcap. The energy resolution for photons with $E_\text{T} \sim 60\,\text{GeV}$ varies between 1.1% and 2.6% over the solid angle of the ECAL barrel, and from 2.2% to 5% in the endcaps [13]. Muons are measured in gas-ionization detectors embedded in the steel flux-return yoke outside the solenoid. Extensive forward calorimetry complements the coverage provided by the barrel and endcap detectors and extends it to $|\eta| < 5$.

The first level (L1) of the CMS trigger system, composed of custom hardware processors, uses information from the calorimeters and muon detectors to select the most interesting events in a fixed time interval of less than 4 μs. The high-level trigger (HLT) processor farm further decreases the event rate from around 100 kHz to around 400 Hz, before data storage. A more detailed description of the CMS detector, together with a definition of the coordinate system used and the relevant kinematic variables, can be found in Ref. [14].

The offline event reconstruction is performed using a particle-flow (PF) algorithm [15, 16]. The PF event reconstruction consists in reconstructing and identifying each single particle with an optimized combination of all subdetector information. The energy of photons is directly obtained from the ECAL measurement, corrected for zero-suppression effects. The energy of electrons is determined from a combination of the electron momentum at the primary interaction vertex as determined by the tracker, the energy of the corresponding ECAL cluster, and the energy sum of all bremsstrahlung photons spatially compatible with originating from the electron track. The energy of muons is obtained from the curvature of the corresponding track. The energy of charged hadrons is determined from a combination of their momentum measured in the tracker and the matching ECAL and HCAL energy deposits, corrected for zero-suppression effects and for the response function of the calorimeters to hadronic showers. The energy of neutral hadrons is obtained from the corresponding corrected ECAL and HCAL energy. Finally, the missing transverse momentum vector $\vec{p}_{\mathrm{T}}^{\,\mathrm{miss}}$ is defined as the projection on the plane perpendicular to the beams of the negative vector sum of the momenta of all reconstructed particles in an event. Its magnitude, the missing transverse energy, is referred to as $\not\!\!E_T$.

For each event, hadronic jets are clustered from these reconstructed particles with the infrared and collinear-safe anti-k_{T} algorithm, operated with a distance parameter of 0.5 [17]. Jet energy corrections are derived from the simulation, and are tuned with in situ measurements with the energy balance of dijet and photon+jet events [18].

3 Event selection

Events for this analysis are collected using a single HLT path, which is seeded by either a 20 GeV or a 22 GeV single e/γ L1 trigger depending on the running period. The HLT is used to select events with at least one photon with $\mathrm{E_T} > 30$ GeV within the ECAL barrel region ($|\eta^{\gamma}| < 1.44$) and calorimetric $\not\!\!E_T$ >25 GeV with noise cleaning to supress the anomalous noise in the HCAL barrel (HB) and endcap (HE) subdetectors due to characteristics of the hybrid photodiodes and the readout boxes [19]. The trigger further requires the photon to pass a loose calorimeter-based isolation selection and to exhibit shower shape characteristics consistent with unconverted photons. The main shower shape requirement is based on the R_9 variable, defined as the ratio of the energy deposited in a 3×3 crystal region centered around the crystal containing an energy deposit greater than all of its immediate neighbours (the "seed crystal") to the energy of the entire deposit of the photon ("supercluster"). The data recorded with this trigger corresponds to an integrated luminosity of 7.3 fb^{-1} and was part of the CMS "data parking" program in 2012. With the data parking program, CMS recorded additional data with relaxed trigger requirements planning for a delayed offline reconstruction in 2013 after the completion of the LHC Run I.

The efficiencies of the trigger as a function of offline reconstructed $\mathrm{E_T^{\gamma}}$ and $\not\!\!E_T$ are measured using two prescaled control trigger paths. The first control trigger path accept events with single photons with energy greater than 30 GeV with no further identification or isolation requirements on the photons. The second control trigger path has identical photon requirements to

the signal path but without any selection on $\not\!\!E_T$. Figure 2 shows the efficiency turn-on curves as a function of E_T^γ and $\not\!\!E_T$, parameterized with an analytic function in the form of:

$$\varepsilon = \frac{p_2}{2} \cdot \left(1 + \mathrm{Erf}\left(\frac{x - p_0}{p_1 \cdot \sqrt{2}}\right)\right). \tag{1}$$

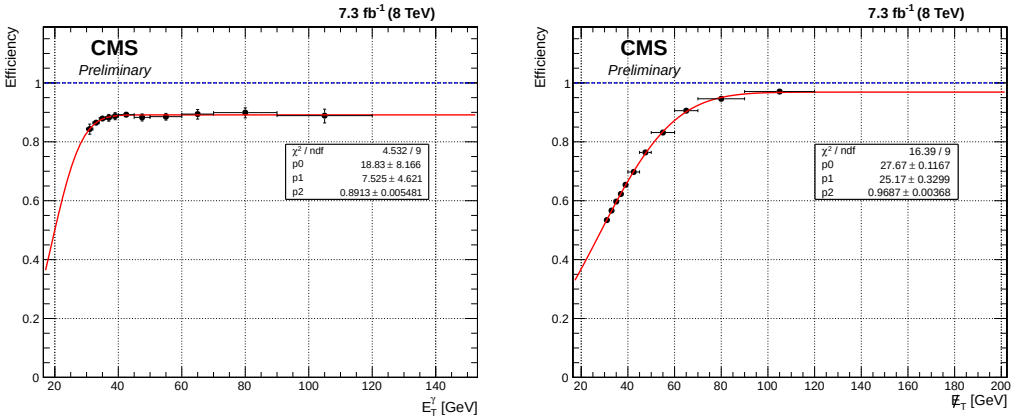

Figure 2: Trigger turn-on curves for E_T^γ and $\not\!\!E_T$. The parameterization of efficiency as a function of offline E_T^γ and $\not\!\!E_T$ are also shown in the form of an analytic function fitted to the turn-on distributions.

In the offline selection, the events are required to have at least one well identified vertex with a distance less than 24 cm away from the nominal interaction point in z-direction and 2 cm away in the xy-plane. The vertex corresponding to the origin of the hard-scattering process with the largest value of $\sum p_T^2$ of all associated tracks is identified as the primary vertex.

Each selected event is required to have at least one photon candidate with $E_T^\gamma > 45\,\mathrm{GeV}$ and $|\eta^\gamma| < 1.44$. The photon must also satisfy the following identification and isolation criteria: (a) to minimize the contribution from misidentified electrons, the shower is required to have no associated hits in the pixel detector, to be referred to as "pixel seed veto"; (b) the lateral extension of the shower, $\sigma_{i\eta i\eta}$, measured in terms of the energy-weighted spread within the 5×5 crystal should be consistent with that of a genuine photon; (c) the ratio between the energy collected by the HCAL cells behind the supercluster and the energy collected by the supercluster is required to be less than 0.05; (d) the sum of the E_T of all photons reconstructed with the particle flow (PF) algorithm within a cone of $\Delta R = 0.3$, excluding a strip in η of 0.015 around the supercluster, is required to be less than $0.7\,\mathrm{GeV} + 0.005\times E_T^\gamma$; (e) the sum of the E_T of all charged hadrons reconstructed with the PF algorithm within a hollow cone of $0.02 < \Delta R < 0.3$ around the supercluster is required to be less than 1.5 GeV; (f) the sum of the E_T of all neutral hadrons reconstructed with the PF algorithm within a cone of $\Delta R = 0.3$ around the supercluster is required to be less than $1.0\,\mathrm{GeV} + 0.04\times E_T^\gamma$. To account for the effects of overlapping proton-proton interactions (pileup), the total energy density in the event is computed using the FastJet package [20] and is used to correct the isolation quantities. These pileup corrected isolation requirements correspond to a working point with a signal efficiency of approximately 85%. Furthermore, $R_9 > 0.9$ is also required to match the trigger requirements. The photon with the highest E_T in the event that satisfies all of the above requirements is selected as the photon candidate for the signal sample.

Anomalous signals in the ECAL, due to direct interaction of particles with the ECAL photo-

diodes, are rejected using additional shower shape requirements on the η and ϕ width of the shower. In addition, we reject showers that deposit more than 95% of their energy on the seed crystal [21].

To reduce the SM backgrounds arising from the leptonic decays of W and Z bosons, a lepton veto is applied. Events are rejected if they have at least one electron fulfilling a loose identification requirement [22] with $p_{\mathrm{T}}^{e} > 10\,\mathrm{GeV}$ and $|\eta^{e}| < 2.5$ (excluding the transition region of $1.44 < |\eta^{e}| \leq 1.55$) and are outside the cone defined by $\Delta R = 0.3$ around the photon candidate. Muons candidates which are identified using the PF algorithm using hits in the tracker and the muon systems are required to have $p_{\mathrm{T}}^{\mu} > 10\,\mathrm{GeV}$, $|\eta^{\mu}| < 2.1$, and $\Delta R(\gamma,\mu) > 0.3$ separation from the photon candidate. Events are rejected if any such muon is present in the event.

In addition to the selection requirements described above, the $\not\!\!E_T$ is required to be greater than 40 GeV. This level of selection is referred to as the preselection and is applied for both the model independent analysis and the analysis of the SUSY benchmark model. The additional applied selection requirements differ between the two analyses.

To define the jet candidates, identification criteria are used to separate pileup jets from the jets originating from hard scattering. These identification criteria are based on the trajectory of tracks associated with the jets inside the tracker volume, the topology of the jet shape and multiplicity of the objects constituting these jets [23]. Only jets with $p_{\mathrm{T}}^{jet} > 30$ GeV and $|\eta^{jet}| < 2.4$ and that fulfill the non-pileup identification requirements are considered in the event. These jets must not overlap with photon candidate within $\Delta R(\gamma,\mathrm{jet}) < 0.5$. In the model independent analysis, events with 2 or more jets are rejected and, if there is a jet in the event, we also require that $\Delta\phi(\gamma,\mathrm{jet}) < 2.5$.

In the analysis of the SUSY benchmark model, where no requirement is made on the jet multiplicity, more advanced selection is applied to reduce the background due to mismeasured $\not\!\!E_T$. Mismeasured $\not\!\!E_T$ can arise from many sources, including limited $\not\!\!E_T$ resolution, reconstruction and instrumental inefficiencies, and improper pattern recognition. Due to their large cross section the $\gamma+$ jets and multijet processes can contribute significantly to the background of this analysis, even though such events do not have genuine $\not\!\!E_T$. In order to minimize the contribution from these processes, we have used two different methods for identifying events with mismeasured $\not\!\!E_T$. The first one is the $\not\!\!E_T$ significance method [24] which takes into account the reconstructed objects in each event and their known measurement resolutions to compute an event-by-event estimation of the likelihood that the observed $\not\!\!E_T$ is consistent with zero. To complement this method we further developed the Missing H_{T} (MH_{T}) minimization method [25]. In the MH_{T} minimization method we first construct a χ^2 function with the form:

$$\chi^2 = \sum_{i=objects} \left(\frac{(p_{\mathrm{T}}^{reco})_i - (\widetilde{p}_{\mathrm{T}})_i}{(\sigma_{p_{\mathrm{T}}})_i} \right)^2 + \left(\frac{\widetilde{\not\!\!E}_x}{\sigma_{\not\!\!E_x}} \right)^2 + \left(\frac{\widetilde{\not\!\!E}_y}{\sigma_{\not\!\!E_y}} \right)^2 . \tag{2}$$

In the above equation, $(p_{\mathrm{T}}^{reco})_i$ are the transverse momenta of the reconstructed objects that pass the above mentioned identification criteria, the $(\sigma_{p_{\mathrm{T}}})_i$ are the expected resolutions of each object, the $\sigma_{\not\!\!E_{x,y}}$ are the resolution of the $\not\!\!E_T$ projection along the x-axis and the y-axis and the $(\widetilde{p}_{\mathrm{T}})_i$ are the free parameters allowed to vary in order to minimize the function. The first term of the equation is a scalar difference. The quantities $\widetilde{\not\!\!E}_{x,y}$ are functions of the free parameters;

$$\widetilde{\not\!\!E}_{x,y} = -\sum_{i=objects} (\widetilde{p}_{x,y})_i \tag{3}$$

In events with no genuine $\not\!\!E_T$, the mismeasured quantities can be re-distributed back into the particle momenta, resulting in a low χ^2 value. On the other hand, in events with genuine $\not\!\!E_T$ from undetected particles, the minimization generally will yield larger χ^2 values. For the analysis of the SUSY benchmark model, the re-calculated $\widetilde{\not\!\!E_T} = \sqrt{\widetilde{\not\!\!E}_x^2 + \widetilde{\not\!\!E}_y^2}$, i.e., in which the original object momenta are replaced with those obtained with the χ^2 minimization, is required to be > 45 GeV and the probability value obtained from the χ^2 minimization is required to be less than 10^{-3}.

To further suppress multijet backgrounds, events are rejected if the scalar sum of transverse momentum of the identified jets ($H_{\rm T}$) in the event is required to be greater than 100 GeV. An additional requirement is made on the angle (α) between the beam direction and the major axis of the supercluster in order to reject photons that have showers elongated along the beam line which is characteristic of non-prompt photons.

Finally, the transverse mass, $M_T = \sqrt{2p_{\rm T}^{\gamma}\not\!\!E_T(1-\cos\Delta\phi(\gamma,\not\!\!E_T))}$, formed by the photon candidate, $\not\!\!E_T$ and the angle between them, is required to be greater than 100 GeV. In order to easily interpret the results within the chosen benchmark model, we require the $\rm E_T^{\gamma}$ <60 GeV.

The final list of advanced selection used in both the model independent analysis and the analysis of the SUSY benchmark model with the relative cumulative efficiencies of the selection requirements relative to the preselection is given on table 1.

Selection requirements	Model ndependent		SUSY benchmark model		
Advanced selection	$Z\gamma \to \nu\bar{\nu}\gamma$	γ+jet	$Z\gamma \to \nu\bar{\nu}\gamma$	γ+jet	$M_{\tilde{\chi}_1^0} = 120\,\text{GeV}$
Number of jets < 2	0.909	0.769	-	-	-
$\Delta\phi(\gamma,\text{jet}) < 2.5$	0.834	0.262	-	-	-
Transverse mass > 100 GeV	-	-	0.867	0.292	0.829
$H_{\rm T} < 100$ GeV	-	-	0.785	0.188	0.804
M$H_{\rm T}$ minimization: $\widetilde{\not\!\!E}_T > 45$ GeV	-	-	0.761	0.071	0.743
M$H_{\rm T}$ minimization: Prob(χ^2)$< 10^{-3}$	-	-	0.626	0.033	0.467
$\not\!\!E_T$ significance > 20	-	-	0.440	0.001	0.195
$\alpha > 1.2$	-	-	0.390	0.001	0.165
$\rm E_T^{\gamma} < 60$ GeV	-	-	0.074	0.0002	0.106

Table 1: Summary of selection for both model independent analysis and analysis with SUSY benchmark model with the cumulative efficiencies of the selection requirements relative to the preselection for $Z\gamma \to \nu\bar{\nu}\gamma$, γ+jet and $M_{\tilde{\chi}_1^0} = 120\,\text{GeV}$.

4 Background estimation

The irreducible background for the $\gamma+\not\!\!E_T$ signal is the SM process $Z\gamma \to \nu\bar{\nu}\gamma$. Other SM backgrounds include Wγ, W $\to$ eν, W $\to \mu\nu$, W $\to \tau\nu$, γ+jet, multijet (referred to as QCD background) and diphoton events. Background events that do not come from collision processes are also considered in the analysis. These backgrounds can be divided broadly into three categories:

- Backgrounds estimated with Monte Carlo (MC) simulation: $Z\gamma \to \nu\bar{\nu}\gamma$, $Z\gamma \to \ell\ell\gamma$, W$\gamma$, γ+jets, $\gamma\gamma$;
- Collision backgrounds estimated using data: jets misidentified as photons and electrons misidentified as photons;

- Non-collision backgrounds estimated using data.

4.1 Background estimates from MC simulation

The $Z\gamma \to \nu\bar{\nu}\gamma$ is the irreducible background in this study. It is estimated from a MC sample generated with MADGRAPH [26] and processed with PYTHIA v6.426 [27] for showering and hadronization. To describe the topology of events in a realistic manner, up to two extra partons were included in the matrix elements during event generation. The final event yields are normalized using the next-to-leading-order (NLO) cross section calculated with the MCFM event generator [28]. The Wγ MC simulation was also produced with MADGRAPH, including up to two extra partons, and normalized using the NLO cross section calculated from MCFM.

The γ+jet is one of the most significant backgrounds in this analysis due to the presence of a genuine photon and the large production cross section. The events for this process are simulated using MADGRAPH, processed through PYTHIA and normalized using the LO cross section. The normalization of this background is then corrected using control sample in data for two different event classes: no-jet and one or more jets. The control sample in data is obtained using events collected with the prescaled single-photon trigger and with the $\not\!\!E_T$ requirement reversed to ensure orthogonality to the signal phase space. Correction factors (C) are derived by normalizing the event yield in the simulation to match the data in the control region, separately for events with zero jets ($C = 1.7$) and one or more jets ($C = 1.1$). These correction factors are then used to normalize the γ+jet event yield from simulation in the signal region. An uncertainty of 16% is derived for these correction factors based on the difference between the corrected and uncorrected simulation and the relative fraction of zero jet ($\sim$ 10% of the events in the control region) and one or more jet events.

The background estimate from the process $Z\gamma \to \ell\ell\gamma$ is obtained using MADGRAPH, and the background estimates from the processes $W \to \mu\nu$, $W \to \tau\nu$ are obtained using PYTHIA. These processes are found to contribute only to a small fraction of the total background prediction.

All simulated events are processed through a GEANT4-based simulation of the CMS detector [29] and the same reconstruction chain as the data. To take into account differences between data and simulation due to imperfect MC modeling, various scale factors (SF) are applied to correct the MC-based estimates. These SFs are defined as the ratio of the efficiency in data to the efficiency in simulation for a given selection. The SF for photon reconstruction and identification is estimated from $Z \to ee$ decays with $R_9 > 0.9$ using a standard "tag-and-probe" method [30] and are listed in Table 2. The trigger efficiency measured in Section 3 is applied to the simulated samples.

Table 2: Scale factors for the photon identification

Variable	E_T^γ $[30-40]$ GeV	E_T^γ $[40-50]$ GeV	$E_T^\gamma > 50$ GeV
Pixel Seed Veto	0.995 ± 0.004	0.970 ± 0.016	1.012 ± 0.014
Photon ID ($0 < \|\eta\| < 0.8$)	0.996 ± 0.010	0.996 ± 0.010	0.996 ± 0.010
Photon ID ($0.8 < \|\eta\| < 1.5$)	0.996 ± 0.010	0.997 ± 0.010	0.997 ± 0.010

4.2 Background estimates from data

The contamination from jets misidentified as photons is estimated by using a data control sample, enriched in QCD multijet events, defined by $\not\!\!E_T < 40$ GeV. In this sample we measure the ratio of events that pass the signal photon identification and isolation criteria (numerator selection) relative to those that pass a looser photon identification and isolation criteria but also fail one of the nominal isolation requirements (denominator selection). The sample of events passing the numerator selection includes genuine photons whose contribution must be subtracted

to obtain the true ratio of misidentified jets. This contribution is estimated by fitting templates of energy-weighted shower widths of genuine photons (determined from MC simulation of γ+jets events) and misidentified photons (determined from an isolation sideband in data) to the candidate distribution. The final corrected extrapolation factor, shown in Figure 3, is then used to scale a sample of events in data which pass the denominator selection in addition to the other non-orthogonal event selections.

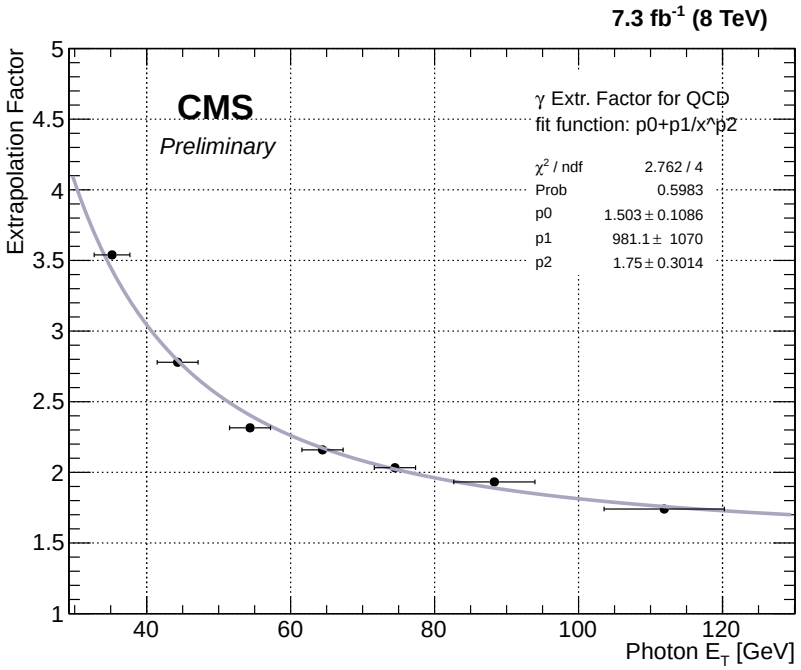

Figure 3: Ratio of number of photons passing signal like requirement relative to those satisfying a very loose identification and isolation selection and at the same time failing at least one of the isolation criteria as a function of E_T^{γ}.

The systematic uncertainty in this method is dominated by the choice of the isolation sideband region and is conservatively estimated to be 35% by varying the charged-hadron isolation in the sideband region definition. The other sources of systematic uncertainty are determined by varying the bin size of the templates, the $\not\!\!E_T$ selection for the control region, and the loose identification requirements on the photons, and are found to be comparatively small.

Events with single electrons misidentified as photons are another major source of background. An electron can be misidentified as a photon if the pixel seed in the tracker from the electron's trajectory does not get reconstructed. This background is estimated using a tag-and-probe method with $Z \to ee$ events. The pixel seed efficiency (ϵ_{γ_e}) to identify electrons is estimated in the Z boson mass window of 60-120 GeV. The inefficiency $(1 - \epsilon_{\gamma_e})$ of the pixel seed requirement is found to be $2.31 \pm 0.03\%$. The ratio $(1 - \epsilon_{\gamma_e})/\epsilon_{\gamma_e}$, which represents the electron misidentification rate, is applied to a candidate sample with the inverted pixel seed requirement and used to estimate the contamination in the signal region. The misidentification rate is found to be dependent on the number of vertices reconstructed in the event and the number of tracks associated to the selected primary vertex. The difference in the final yields using the two parameterizations or the inclusive measurement of ϵ_{γ_e} are found to be within 5%. This difference is considered as a systematic uncertainty, and the yield calculated using the inclusive rate is used as the nominal estimate. The method is repeated on simulation, and the difference of 4% between the measured and known electron misidentification rate is considered as

an additional source of systematic uncertainty.

4.3 Non-collision background estimates from data

The search is susceptible to contamination from non-collision backgrounds which arise from cosmic ray interactions, spurious signals in the ECAL, and accelerator induced secondary particles (beam halo). These backgrounds have different arrival time distributions compared to prompt photons produced in hard scattering. To quantify the contamination due to these backgrounds a fit is performed to the candidate time distribution using background templates derived from the data. The contamination due to out-of-time background contribution is found to be negligible, therefore not included in the final event yield.

4.4 Background modeling validation

The background modeling is examined in several control regions. A control sample enriched in $W(l\nu)\gamma$ events is defined with inverted lepton-veto requirement in the preselection, thus selecting events with a loose e or μ. It is expected to be free of any signal contamination due to the presence of a lepton. Another control sample enriched in γ+jet events is constructed by just requiring no selection other than the preselection requirements. Figure 4 shows the data vs SM expectation in the two control regions. The observed data and estimated SM backgrounds are found to be consistent both in yield and shape.

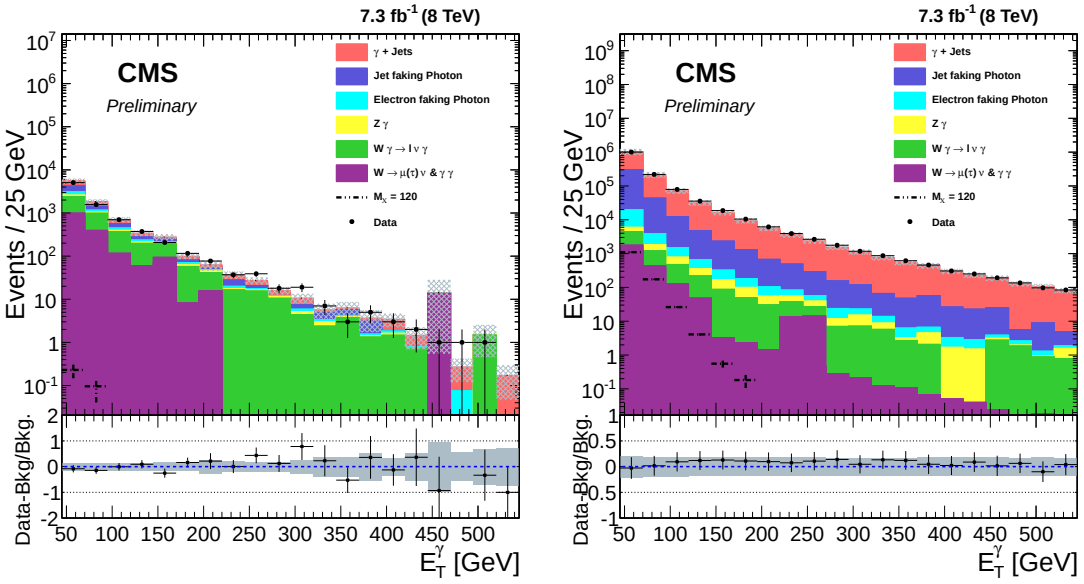

(a) (b)

Figure 4: The E_T^γ distributions for data vs. SM expectation in a control region enriched by (a) W($l\nu$) events, and (b) γ+jet events. The bottom panels in each plot show the ratio of (data - background)/background and the gray band includes both the statistical and systematic uncertainty on the background prediction.

5 Systematic uncertainties

The experimental systematic uncertainties considered in the analysis are listed in Table 3. Since the model independent and model specific selections differ significantly, e.g. the inclusion

of the mismeasured $\not\!\!E_T$ reduction selection and E_T^γ window for the model specific results, the systematic uncertainties are evaluated separately for each selection. The systematic uncertainty associated with the measurement of the integrated luminosity is 2.6% [31]. The photon energy scale uncertainty [32] of about 1.0% affects the signal and background predictions by 4% for the model specific selection and by 0.5% for the model independent selection. Similarly, the jet energy scale uncertainty affects the signal and background predictions by $2-5$% depending on the process and selection. When varying the photon or jet energy scales, the $\not\!\!E_T$ is also recomputed. In addition, the systematic uncertainty associated with the jet energy resolution (0.5%) and unclustered energy (energy not contained within jets or leptons or photons) scale (2%) are propagated to the $\not\!\!E_T$ and effect the signal and background predictions by $2-4$%. The uncertainty due to the choice of parton density functions (PDFs) is estimated following PDF4LHC recommendations [33–35] and are found to be 10% for SUSY Higgs boson signal, and 4% for $Z\nu\nu\gamma$ and the $W\gamma$. An additional uncertainty due to the choice of renormalization and factorization scales is evaluated using MCFM and is found to be 3% for $Z\nu\nu\gamma$ and the $W\gamma$. As described in the previous section, a 16% uncertainty is applied to the γ+jet normalization due to the difference in the jet multiplicity distribution between the data and background prediction in the γ+jet control region. The uncertainty due to the pileup modeling is found to be 1% and is estimated by shifting the central value of the total inelastic cross section from 69.4 mb to 73.5 mb. Finally, the systematic uncertainties associated with backgrounds estimated from data have been applied as discussed in previous section.

Source	Signal	Jet$\rightarrow\gamma$	Electron$\rightarrow\gamma$	γ + jet	$Z\nu\nu\gamma$	$W\gamma$
PDF	10(0)	-	-	-	4(4)	4(4)
Luminosity	2.6(2.6)	-	-	2.6(2.6)	2.6(2.6)	2.6(2.6)
Photon energy scale $\pm$ 1 %	4(0.5)	-	-	4(0.5)	4(0.5)	4(0.5)
$\not\!\!E_T$ energy scale	4(2)	-	-	4(2)	4(2)	4(2)
Jet energy scale	3(2)	-	-	5(5)	3(2)	3(2)
Pileup	1(1)	-	-	1(1)	1(1)	1(1)
$Z\nu\nu\gamma$ MCFM NLO calculation	-	-	-	-	3(3)	-
$\gamma+$ jet normalization	-	-	-	16(16)	-	-
$W\gamma$ MCFM NLO calculation	-	-	-	-	-	3(3)
Jet$\rightarrow\gamma$ unc.	-	35(35)	-	-	-	-
Electron$\rightarrow\gamma$ unc.	-	-	6(6)	-	-	-

Table 3: Summary of all systematic relative uncertainties in percent on $A \times \epsilon_{MC}$ calculation for SUSY Higgs model (Model independent) selection.

6 Results

To evaluate the 95% confidence level (CL) limits on the new physics production cross section, an asymptotic CL_S method [36, 37] is used where the systematic uncertainties in the signal and background predictions are treated as nuisance parameters with log-normal prior distributions.

6.1 Model-independent limits

Due to the variety of signals which can contribute to this final state, we present results for a generic signal using the model-independent selection described in Section 3. Although this selection does not have as strong of discrimination power between signal like and background like events compared to the misreconstructed $\not\!\!E_T$ rejection selections, it does have less model dependence. This is due to $\not\!\!E_T$ significance and $\tilde{\not\!\!E}_T$ minimization requirements having a non trivial efficiency dependence on the underlying event and observed $\not\!\!E_T$.

The total expected SM background and observed data events after the model-independent selection are found to be compatible within the systematic uncertainties. Table 4 shows a comparison of the event yields estimated for background processes and the observed data. Figure 5 shows the M_T and $\not{E}_T$ distributions after the model-independent selection has been applied.

Process	of Events
$\gamma+$ jets	$(313 \pm 50) \times 10^3$
jet $\rightarrow \gamma$	$(906 \pm 317) \times 10^2$
e $\rightarrow \gamma$	$(1035 \pm 62) \times 10^1$
$W(\rightarrow \ell\nu) + \gamma$	2239 ± 111
$Z(\rightarrow \nu\bar{\nu}) + \gamma$	2050 ± 102
Other	1809 ± 91
Total background	$(420 \pm 82) \times 10^3$
Data	442×10^3

Table 4: Comparison of event yields for observed data and background, after the model-independent selection.

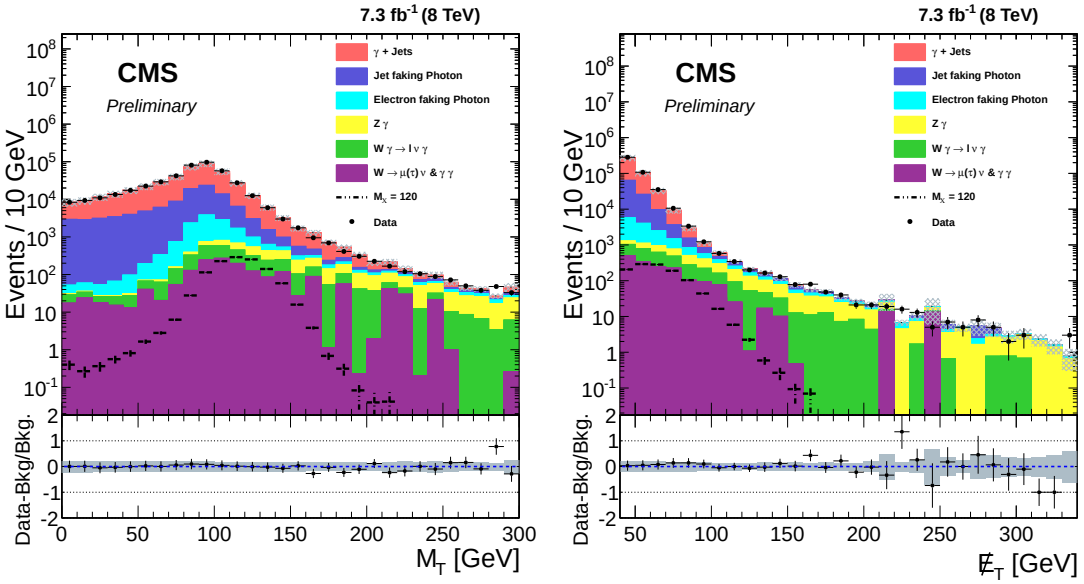

(a) (b)

Figure 5: The M_T and $\not{E}_T$ distributions for data, background estimates, and signal after the model-independent selection. The bottom panels in each plot show the ratio of (data - background)/background and the gray band includes both the statistical and systematic uncertainty on the background prediction.

Figure 6 shows the observed and expected model-independent 95% CL upper limits on $\sigma \times BR \times A \times \epsilon$ for different $\not{E}_T$ and M_T thresholds. The observed and expected limits are also shown in Fig 6(c) at a 95% CL for $M_T > 100$ GeV and as a function of $\not{E}_T$.

6.2 Model-specific limits

The yields for supersymmetric decays of the Higgs boson ($h \rightarrow \widetilde{G}\tilde{\chi}_1^0, \tilde{\chi}_1^0 \rightarrow \widetilde{G}\gamma$) are acquired through imposing the model-specific selection described in Section 3. The yields for this selection are shown in Table 5. The 95% CL upper limits on the $\sigma\times$ branching ratio(BR) and

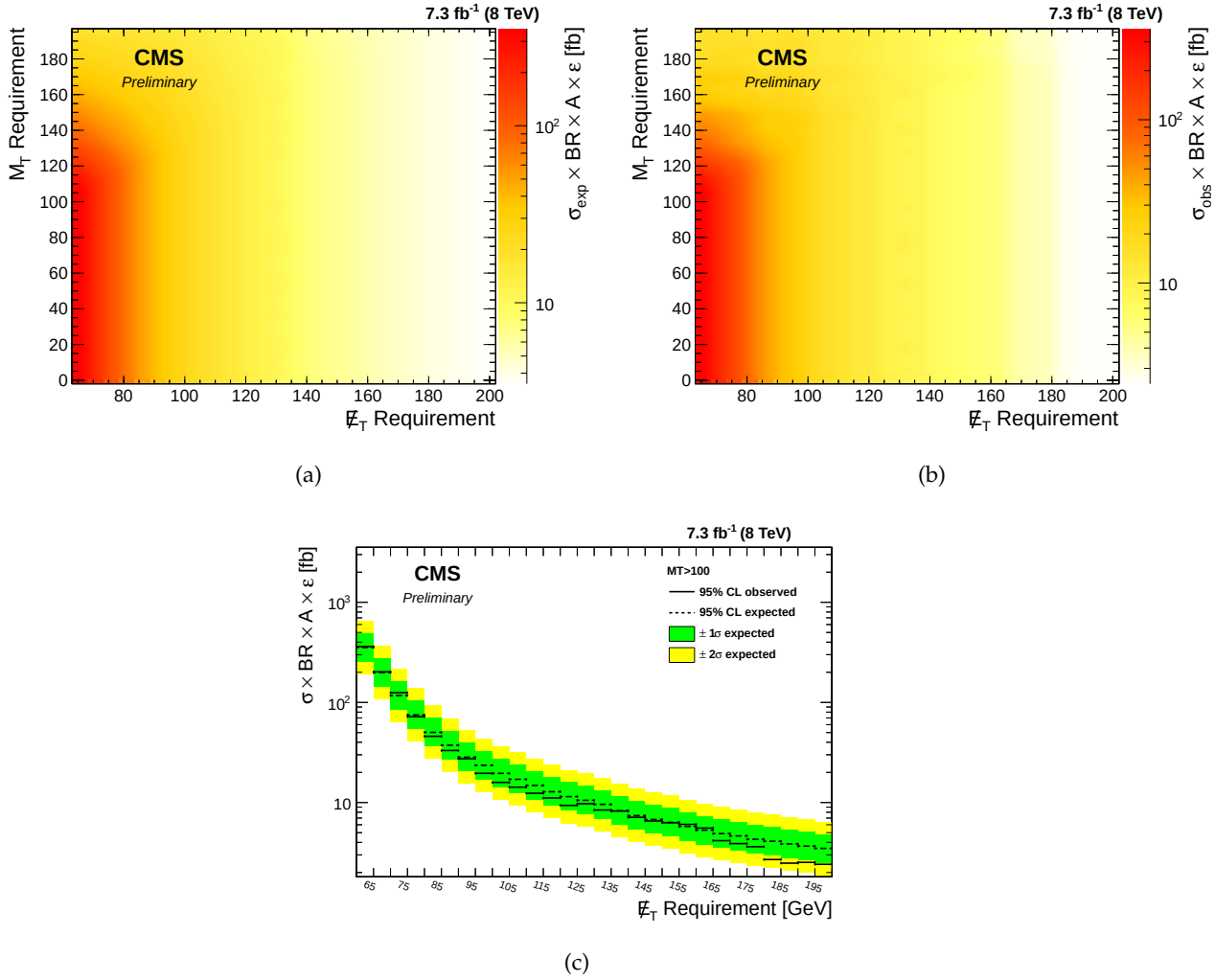

Figure 6: The expected (a) and observed (b) 95% CL upper limit on $\sigma \times BR \times A \times \epsilon$ for different M_T and $\not\!\!E_T$ thresholds and (c) for $M_T > 100$ GeV as function of the $\not\!\!E_T$ threshold.

$(\sigma \times BR)/\sigma_{SM}$, where σ_{SM} is the cross section for the standard model Higgs boson, are evaluated for different mass values of $\widetilde{\chi}_1^0$ ranging from 65 GeV to 120 GeV and are shown in Fig. 7.

7 Conclusions

A search for new physics in the $\gamma+\not\!\!E_T$ final state is performed using pp collision data corresponding to an integrated luminosity of 7.3 fb^{-1} collected at $\sqrt{s} = 8$ TeV using data parking triggers in a phase space region defined by $E_T > 45$ GeV and $\not\!\!E_T > 40$ GeV. In the absence of any evidence of new physics, upper limits are placed on the production cross section of new physics in a model-independent way for different $\not\!\!E_T$ and M_T thresholds. The data are also examined using optimized selections for maximum sensitivity to an exotic decay of the Higgs boson $h \to \widetilde{G}\widetilde{\chi}_1^0, \widetilde{\chi}_1^0 \to \widetilde{G}\gamma$ predicted in a low-scale SUSY breaking scenario. Upper limits at 95% CL are placed on the new physics production cross section times the branching ratio, as well as the ratio of this product to the SM Higgs boson production cross section. The results are found to be compatible with the SM hypothesis. These results are the first limits on this model from searches at pp colliders.

Process	Estimate
$\gamma+$ jets	179 ± 28
jet $\to \gamma$	269 ± 94
e $\to \gamma$	355 ± 28
$W(\to \ell\nu) + \gamma$	154 ± 15
$Z(\to \nu\bar{\nu}) + \gamma$	182 ± 13
Other	91 ± 10
Total background	1232 ± 188
Data	1296
$M_{\tilde{\chi}_1^0} = 65$ GeV	653.0 ± 77
$M_{\tilde{\chi}_1^0} = 95$ GeV	1158.1 ± 137
$M_{\tilde{\chi}_1^0} = 120$ GeV	2935.0 ± 349

Table 5: Expected (SM background) and observed event yields after the selection optimized for the supersymmetric decay of the Higgs boson ($h \to \tilde{G}\tilde{\chi}_1^0, \tilde{\chi}_1^0 \to \tilde{G}\gamma$) and the signal predictions correspond to BR(H $\to$ *invisible* $+ \gamma$) = 100%.

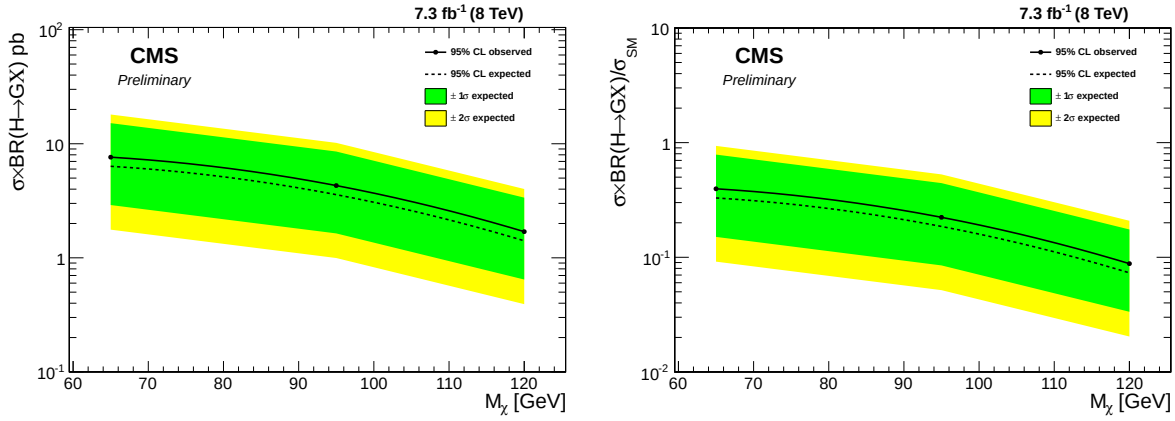

(a) (b)

Figure 7: Expected and observed 95% CL upper limits on (a) $\sigma \times BR$ and (b) the ratio of this product over the SM Higgs production cross section as a function of different $M_{\tilde{\chi}_1^0}$ values. The uncertainty on the expected limit at 1σ and 2σ levels are shown as green and yellow bands, respectively.

References

[1] P. Fayet, "Mixing Between Gravitational and Weak Interactions Through the Massive Gravitino", *Phys. Lett.* **B70** (1977) 461, doi:10.1016/0370-2693(77)90414-2.

[2] H. Baer, M. Brhlik, C. H. Chen, and X. Tata, "Signals for the Minimal Gauge-Mediated Supersymmetry Breaking Model at the Fermilab Tevatron Collider", *Phys. Rev.* **D55** (1997) 4463, doi:10.1103/PhysRevD.55.4463.

[3] H. Baer, P. G. Mercadante, X. Tata, and Y. L. Wang, "Reach of Tevatron Upgrades in Gauge-Mediated Supersymmetry Breaking Models", *Phys. Rev.* **D60** (1999) 055001, doi:10.1103/PhysRevD.60.055001.

[4] S. Dimopoulos, S. Thomas, and J. D. Wells, "Sparticle Spectroscopy and Electroweak Symmetry Breaking with Gauge-Mediated Supersymmetry Breaking", *Nucl. Phys.* **B488**

(1997) 39, doi:10.1016/S0550-3213(97)00030-8.

[5] J. R. Ellis, J. L. Lopez, and D. V. Nanopoulos, "Analysis of LEP Constraints on Supersymmetric Models with a Light Gravitino", *Phys. Lett.* **B394** (1997) 354, doi:10.1016/S0370-2693(97)00019-1.

[6] M. Dine, A. Nelson, Y. Nir, and Y. Shirman, "New Tools for Low Energy Dynamical Supersymmetry Breaking", *Phys. Rev.* **D53** (1996) 2658, doi:10.1103/PhysRevD.53.2658.

[7] G. F. Giudice and R. Rattazzi, "Gauge-Mediated Supersymmetry Breaking", in *Perspectives on Supersymmetry*, p. 355. World Scientific, Singapore, 1998.

[8] CMS Collaboration, "Observation of a new boson at a mass of 125 GeV with the CMS experiment at the LHC", *Physics Letters B* **716** (2012) 30, doi:10.1016/j.physletb.2012.08.021.

[9] ATLAS Collaboration, "Observation of a new particle in the search for the Standard Model Higgs boson with the ATLAS detector at the LHC", *Physics Letters B* **716** (2012) 1, doi:10.1016/j.physletb.2012.08.020.

[10] C. Petersson, A. Romagnoni, and R. Torre, "Higgs Decay with Monophoton + MET Signature from Low Scale Supersymmetry Breaking", *JHEP* **10** (2012) 016, doi:10.1007/JHEP10(2012)016, arXiv:1203.4563.

[11] CMS Collaboration, "Search for Dark Matter and Large Extra Dimensions in pp Collisions Yielding a Photon and Missing Transverse Energy", *Phys.Rev.Lett.* **108** (2012) 261803, doi:10.1103/PhysRevLett.108.261803, arXiv:1204.0821.

[12] ATLAS Collaboration, "Search for dark matter candidates and large extra dimensions in events with a photon and missing transverse momentum in pp collision data at $\sqrt{s} = 7$ TeV with the ATLAS detector", *Phys.Rev.Lett.* **110** (2013) 011802, doi:10.1103/PhysRevLett.110.011802, arXiv:1209.4625.

[13] CMS Collaboration, "Energy Calibration and Resolution of the CMS Electromagnetic Calorimeter in pp Collisions at $\sqrt{s} = 7$ TeV", *JINST* **8** (2013) P09009, doi:10.1088/1748-0221/8/09/P09009, arXiv:1306.2016.

[14] CMS Collaboration, "The CMS experiment at the CERN LHC", *JINST* **3** (2008) S08004, doi:10.1088/1748-0221/3/08/S08004.

[15] CMS Collaboration, "Particle–Flow Event Reconstruction in CMS and Performance for Jets, Taus, and $E_{\mathrm{T}}^{\mathrm{miss}}$", CMS Physics Analysis Summary CMS-PAS-PFT-09-001, 2009.

[16] CMS Collaboration, "Commissioning of the Particle-flow Event Reconstruction with the first LHC collisions recorded in the CMS detector", CMS Physics Analysis Summary CMS-PAS-PFT-10-001, 2010.

[17] M. Cacciari, G. P. Salam, and G. Soyez, "The anti-k_t jet clustering algorithm", *JHEP* **04** (2008) 063, doi:10.1088/1126-6708/2008/04/063, arXiv:0802.1189.

[18] CMS Collaboration, "Determination of the Jet Energy Scale in CMS with pp Collisions at $\sqrt{s} = 7$ TeV", CMS Physics Analysis Summary CMS-PAS-JME-10-010, 2010.

[19] A. Apresyan on behalf of CMS Collaboration, "Identification and mitigation of anomalous signals in CMS HCAL", CMS Conference Report CMS-CR-2012-238, 2012.

[20] M. Cacciari, G. P. Salam, and G. Soyez, "FastJet User Manual", *Eur.Phys.J.* **C72** (2012) 1896, doi:10.1140/epjc/s10052-012-1896-2, arXiv:1111.6097.

[21] W. Bialas, D.A. Petyt on behalf of CMS Collaboration, "Mitigation of anomalous APD signals in the CMS ECAL", *JINST* **8** (2013) C03020, doi:10.1088/1748-0221/8/03/C03020.

[22] CMS Collaboration, "Performance of electron reconstruction and selection at the CMS detector at $\sqrt{s}$=8 TeV", paper in preparation.

[23] CMS Collaboration, "Pileup Jet Identification", CMS Physics Analysis Summary CMS-PAS-JME-13-005, 2013.

[24] CMS Collaboration, "Missing transverse energy performance of the CMS detector", *JINST* **6** (2011) P09001, doi:10.1088/1748-0221/6/09/P09001, arXiv:1106.5048.

[25] CMS Collaboration Collaboration, "Search for new phenomena in monophoton final states in proton-proton collisions at $\sqrt{s}$ = 8 TeV", arXiv:1410.8812.

[26] J. Alwall et al., "MadGraph 5 : Going Beyond", *JHEP* **06** (2011) 128, doi:10.1007/JHEP06(2011)128, arXiv:1106.0522.

[27] T. Sjöstrand, S. Mrenna, and P. Skands, "PYTHIA 6.4 physics and manual", *JHEP* **05** (2006) 026, doi:10.1088/1126-6708/2006/05/026, arXiv:hep-ph/0603175.

[28] J. Campbell, R. Ellis, and C. Williams, "MCFM v6.1: A Monte Carlo for FeMtobarn processes at Hadron Colliders", 2011, http://mcfm.fnal.gov/mcfm.pdf.

[29] GEANT4 Collaboration, "GEANT4–a simulation toolkit", *Nucl. Instrum. Meth.* **A 506** (2003) 250, doi:10.1016/S0168-9002(03)01368-8.

[30] CMS Collaboration, "Measurement of the Inclusive W and Z Production Cross Sections in pp Collisions at $\sqrt{s} = 7$ TeV", *JHEP* **10** (2011) 132, doi:10.1007/JHEP10(2011)132, arXiv:1107.4789.

[31] CMS Collaboration, "CMS Luminosity Based on Pixel Cluster Counting - Summer 2013 Update", CMS Physics Analysis Summary CMS-PAS-LUM-13-001, 2013.

[32] CMS Collaboration, "Performance of photon reconstruction and identification in proton-proton collisions at $\sqrt{s}$ = 8 TeV", paper in preparation.

[33] M. Botje et al., "The PDF4LHC Working Group Interim Recommendations", (2011). arXiv:1101.0538.

[34] R. D. Ball et al., "Impact of Heavy Quark Masses on Parton Distributions and LHC Phenomenology", *Nucl. Phys.* **B 849** (2011) 296–363, doi:10.1016/j.nuclphysb.2011.03.021, arXiv:1101.1300.

[35] A. Martin, W. Stirling, R. Thorne, and G. Watt, "Parton distributions for the LHC", *Eur. Phys. J. C* **63** (2009) 189, doi:10.1140/epjc/s10052-009-1072-5, arXiv:0901.0002.

[36] A. L. Read, "Presentation of search results: The CL(s) technique", *J. Phys.* **G 28** (2002) 2693, doi:10.1088/0954-3899/28/10/313.

[37] T. Junk, "Confidence level computation for combining searches with small statistics", *Nucl. Instrum. Meth.* **A 434** (1999) 435–443, doi:10.1016/S0168-9002(99)00498-2, arXiv:hep-ex/9902006.